INVITED ARTICLE

The influence of arm composition on the self-assembly of low-functionality telechelic star polymers in dilute solutions

Esmaeel Moghimi[1,2] · Iurii Chubak[3] · Dimitra Founta[1,2] · Konstantinos Ntetsikas[4] · George Polymeropoulos[4] · Nikos Hadjichristidis[4] · Christos N. Likos[3] · Dimitris Vlassopoulos[1,2]

Abstract

We combine synthesis, physical experiments, and computer simulations to investigate self-assembly patterns of low-functionality telechelic star polymers (TSPs) in dilute solutions. In particular, in this work, we focus on the effect of the arm composition and length on the static and dynamic properties of TSPs, whose terminal blocks are subject to worsening solvent quality upon reducing the temperature. We find two populations, single stars and clusters, that emerge upon worsening the solvent quality of the outer block. For both types of populations, their spatial extent decreases with temperature, with the specific details (such as temperature at which the minimal size is reached) depending on the coupling between inter- and intra-molecular associations as well as their strength. The experimental results are in very good qualitative agreement with coarse-grained simulations, which offer insights into the mechanism of thermoresponsive behavior of this class of materials.

Keywords Gels · Micelles · Nanoparticles · Polymer brushes · Polymer synthesis · Properties · Mechanical · Properties · Thermal · Self-assembly

Introduction

Self-organization of building blocks due to external stimuli is ubiquitous in most materials and all living organisms in nature. Inspired by this, a remarkable body of work has been performed to understand and emulate their response to temperature [1–3], pH [4–6] and light [7, 8], enabling

E. M. and I. C. contributed equally.

✉ Christos N. Likos
  christos.likos@univie.ac.at

✉ Dimitris Vlassopoulos
  dvlasso@iesl.forth.gr

[1] Institute of Electronic Structure and Laser, FORTH, 71110, Heraklion, Crete, Greece

[2] Department of Materials Science, Technology, University of Crete, 71003, Heraklion, Crete, Greece

[3] Faculty of Physics, University of Vienna, Boltzmanngasse 5, A-1090, Vienna, Austria

[4] Physical Sciences and Engineering Division, KAUST Catalysis Center, Polymer Synthesis Laboratory, King Abdullah University of Science and Technology (KAUST), Thuwal, 23955, Kingdom of Saudi Arabia

the controlled design of their structure assembly. Recent advances in polymer chemistry have led to the synthesis of various building blocks with complex architectures and functionalized properties. Such responsive building blocks that can self-organize into higher-order structures may form soft patchy particles, which have directional interactions and varying softness. Furthermore, topological effects that arise in systems with complex architecture can alone lead to a range of interesting phenomena in and out of thermodynamic equilibrium for both low [9–15] and high system densities [16–21]. Functionalized biomolecules such as DNA-grafted colloidal particles represent a typical example where patchiness reflects the competition between inter- and intra-particle associations [22–25]. However, despite its significance, DNA-based research is very specialized and yields limited amounts of samples. An alternative design of patchy particles is based on the so-called Telechelic Star Polymers (TSPs), that is star polymers with functionalized end groups [26–29]. A TSP consists of f amphiphilic AB-block copolymer arms grafted on a common center. The solvophilic A-block is attached at the center of the star, whereas the solvophobic B-block is exposed to the exterior of the star. On changing the solvent quality through temperature variation, the outer blocks become attractive and form patches on the surface

of the particle [30–32]. With such a TSP system, it is thus possible to cover the entire range of inter-particle interactions, from purely repulsive to attractive soft colloids simply by changing the solvent quality. The self-assembly of TSPs at the single molecule level and in concentrated solutions depends mainly on three parameters: (*i*) the functionality f of the stars, (*ii*) the outer block size ratio $\alpha = N_B/(N_A + N_B)$ (N_A and N_B denote the length of the respective block), and (*iii*) the attraction strength between the outer solvophobic blocks which is enhanced upon worsening solvent quality.

TSPs with low functionality ($f \leq 5$) collapse into a watermelon structure with one single patch on the surface of the particle [30]. However, more complex structures with a richer distribution of patches are formed in TSPs with higher functionality [31]. Such soft patchy particles can preserve their properties such as the size, number, and arrangement of patches upon increasing the TSP concentration [33]. The inherent flexibility of such soft-particles leads to formation of ordered structures in the case of high functionality [33]. On the other hand, low-functionally TSPs tend to form micellar aggregates [34–37], which at relatively high concentrations self-assemble into long worm-like micelles [35, 38]. In previous work, we have examined the effects of temperature (or attraction strength) on the self-assembly of these low-f TSPs in dilute solution [32]. In the present work, we extend these investigations by addressing the effects of the block size ratio and arm length on the self-organization of TSPs with $f = 3$ in dilute solutions. The new results provide insight into the responsive behavior of TSPs, paving the way for the design of functional materials with tunable properties.

Materials and methods

Experimental details

Telechelic star polymers (TSPs) with three arms made of 1,4-polybutadiene (PB) as the inner A-block and polystyrene (PS) as the outer B-block were synthesized by anionic polymerization and chlorosilane chemistry using high-vacuum techniques. Detailed information on the synthesis procedure can be found in Ref. [32]. Three different TSP samples have been used in the present study. Two of them have a similar total molar mass of about 40000 g/mol, albeit a different PS weight fraction of $f_{PS} = 0.14$ and 0.33. The third sample, which was used in our previous work [32], has a lower molar mass of $M_W = 26700$ g/mol and $f_{PS} = 0.23$. The molar mass distribution in all three TSP samples is rather narrow with the corresponding polydispersity being around Đ = 1.03. The detailed molecular characteristics of the samples are listed in Table 1.

We have used 1-phenyldodecane as the solvent. It has a cloud-point at 53 °C for PS [39] and 22 °C for PB (the corresponding θ-temperatures are expected to be slightly higher). Solutions were prepared by mixing an appropriate amount of the TSP with the solvent to reach the desired concentration. The sample degradation was inhibited by adding 0.1 wt% of the TSP of the antioxidant BHT (2,6-Di-tert-butyl-4-methylphenol). In order to fully dissolve TSPs, methylene chloride was used as the cosolvent. Then, the cosolvent was evaporated under ambient conditions until a constant weight was achieved.

Dynamic Light Scattering (DLS) was used to investigate the dynamics and self-assembly of TSPs in dilute solutions. In DLS, the normalized autocorrelation function $G(q, t) = \langle I(q, 0) I(q, t) \rangle / \langle I(q, 0) \rangle^2$ of the total scattered light intensity $I(q)$ at the wave vector $q = (4\pi n_0/\lambda) \sin(\theta/2)$ (n_0 is the refractive index, θ denotes the scattering angle, and λ is the wavelength of the incident laser beam) is related to the normalized time correlation function of the scattered electric field $E(q, t)$ by the Siegert relation:

$$G(q, t) = 1 + f^* |\tilde{\alpha} g(q, t)|^2 = 1 + f^* |C(q, t)|^2, \quad (1)$$

where f^* stands for the coherence instrumental factor, $\tilde{\alpha}$ is the fraction of $I(q)$ associated with fluctuations relaxing with times longer than 0.1 μs [40–42], and $C(q, t)$ denotes the intermediate scattering function (ISF). The inverse Laplace transformation using the constrained regularization method was applied to compute the relaxation spectrum

Table 1 Molecular characteristics of investigated star diblock copolymers (PS-b-PB)$_3$

Sample	M_w^{star} (g/mol)	M_w^{linear} (g/mol)	f_{PS} %(w/w)	f_{PB} %(w/w)	c/c^*	n (mol/m^3)
1	40500	13000	0.14	0.86	0.03	0.14
2	40000	13000	0.33	0.67	0.04	0.11
3	26700	8800	0.23	0.77	0.05	0.31

M_w^{star} is the total molar mass of the TSP, M_w^{linear} is the arm molar mass, f_{PS} and f_{PB} are the weight fractions of PS and PB blocks, respectively. c is the TSP concentration in terms of the overlap concentration $c^* = 3M_w^{star}/(4\pi R_h^3 \mathcal{N}_A)$ (R_h is the star's hydrodynamic radius at high temperatures and $\mathcal{N}_A$ is the Avogadro number), and n is the number density of TSPs in solution

$H(\ln \tau)$. This method assumes that $C(q, t)$ can be expressed as the superposition of exponentials:

$$C(q, t) = \int_{-\infty}^{+\infty} H(\ln \tau) \exp(-t/\tau) \, d(\ln \tau) \tag{2}$$

The characteristic relaxation times correspond to the peak positions of $H(\ln \tau)$, whereas the area under the peak defines the value of $\tilde{\alpha}$ in Eq. 1 and hence the intensity $\tilde{\alpha} I(q)$ associated with the particular dynamic process. The transformation was performed with the program CONTIN [43] that yielded the relaxation time and intensity of the partitioning modes.

DLS experiments were performed on an ALV-5000 goniometer/correlator setup (ALV-GmbH, Germany). The light source was a Nd:YAG dye-pumped, air-cooled laser (100 mW) with the wavelength $\lambda = 532$ nm. The refractive index of 1-phenyldodecane is $n_0 = 1.482$. Before each DLS experiment, the samples were equilibrated at $T = 60\,°C$, which is above the cloud point of the outer PS-block, for 10 min to erase thermal history. Then, the sample was quenched to the desired temperature and equilibrated. The equilibration process was probed by measuring the ISF until it reached steady values over time. The duration of equilibration depended on the temperature and ranged from 10 min for $T = 60\,°C$ to 10 h for $T = 20\,°C$.

Simulation details

To model TSP dynamics under worsening solvent conditions for its outer block, we have employed a coarse-grained dissipative particle dynamics (DPD) model with explicit solvent. In what follows, the inner blocks of a TSP are labeled "A," the outer ones—"B," whereas solvent particles—"S." In DPD, the total force $\mathbf{F}_i$ acting on the ith particle is composed of the conservative $\mathbf{F}^C$, dissipative $\mathbf{F}^D$, and random $\mathbf{F}^R$ contributions [44]:

$$\mathbf{F}_i = \sum_{j \neq i} \left(\mathbf{F}_{ij}^C + \mathbf{F}_{ij}^D + \mathbf{F}_{ij}^R \right). \tag{3}$$

In Eq. 3 above, $\mathbf{F}_{ij}^C$ is the conservative force acting between the ith and jth particle separated by a distance r_{ij} (here and in what follows, $\mathbf{r}_{ij} = \mathbf{r}_i - \mathbf{r}_j$, $r_{ij} = |\mathbf{r}_{ij}|$, $\hat{\mathbf{r}}_{ij} = \mathbf{r}_{ij}/r_{ij}$, and $\mathbf{v}_{ij} = \mathbf{v}_i - \mathbf{v}_j$):

$$\mathbf{F}_{ij}^C = A_{ij} w(r_{ij}), \tag{4}$$

where A_{ij} is the maximal repulsion between the particles and $w(r_{ij})$ is given by

$$w(r_{ij}) = (1 - r_{ij}/r_{cut}) \theta(r_{cut} - r), \tag{5}$$

with $\theta(x)$ denoting the Heaviside step function and the cutoff distance r_{cut} being chosen as the unit of length ($r_{cut} = 1$). Furthermore, $\mathbf{F}_{ij}^D$ is the pairwise dissipative force

$$\mathbf{F}_{ij}^D = -\gamma w(r_{ij})^2 \left(\hat{\mathbf{r}}_{ij} \cdot \mathbf{v}_{ij} \right), \tag{6}$$

and $\mathbf{F}_{ij}^R$ is the pairwise random force

$$\mathbf{F}_{ij}^R = -\sqrt{2\gamma k_B T/\Delta t} \cdot \eta_{ij} w(r_{ij}), \tag{7}$$

where η_{ij} is a Gaussian random number with zero mean and unit variance. The unit of mass is set by the (same) mass of every particle m, whereas the unit of energy was chosen to be $k_B T$ ($k_B T = 1$). The simulation were performed using the HOOMD-blue simulation package [45–48] using friction coefficient $\gamma = 4.5 m\tau^{-1}$ and the equations of motion were integrated using the Velocity-Verlet algorithm [49] with time step $\Delta t = 0.04\tau$, where $\tau = r_{cut}\sqrt{m/k_B T}$ is the DPD unit of time.

To obtain the total polymerization degree N of the star arms in the experimental samples considered, we first estimated the molar volumes of PB and PS, given by $v_{PS/PB} = M_W/\rho_{PS/PB}$, where $\rho_{PS/PB}$ is the corresponding molar density ($\rho^{PS} = 1.05$ g/mL and $\rho^{PB} = 0.892$ g/mL). N and $\alpha_{PS/PB}$ were then computed on the basis of the PS reference segment volume 99.2 mL/mol and are listed in Table 2. In general, we are interested in the behavior of experimental systems in a rather narrow temperature range $20\,°C < T < 60\,°C$, where the Flory-Huggins incompatibility parameter $\chi_{PS\text{-}PB} = 18.78/T - 9.6 \cdot 10^{-4}$ [50] does not change substantially (experimental values of $\chi_{PS\text{-}PB} N$ for the three samples in such temperature range are $\chi_{PS\text{-}PB} N \lesssim 10$), implying that the self-assembly is mainly controlled by the solvent selectivity towards the outer block.

Given the computational cost of simulations with explicit solvent particles, we focused on a star polymer model with $f = 3$ arms containing $N = 64$ monomers, and systematically varied the outer block ratio α by changing N_A and N_B. All our simulations were performed at total particle density $\rho r_{cut}^3 = 3$. Bonded interactions were given by $V_{bond}(r) = \frac{K}{2}(r - r_{cut})^2$ with $K = 50 k_B T$. The central particle, to which all arms were connected to, was treated as a monomer of type A. In DPD, repulsion amplitudes A_{ij} can be directly related to the Flory-Huggins χ_{ij} parameters [51]:

$$A_{ij} \approx A_{ii} + \kappa(\rho) \chi_{ij}, \tag{8}$$

where $\kappa(\rho)$ depends on the DPD density such that $\kappa(3) = 3.49$. In all simulations, we fixed the inter-block incompatibility parameter $\chi_{AB} = 0.23$, which corresponds to $A_{AB} = 25.8$ at $\rho r_{cut}^3 = 3$. Such value of χ_{AB} was obtained from a conservative experimental value $(\chi_{AB} N)_{exp} = 10$ by taking into account finite polymer chain length corrections: $\chi_{AB} = (\chi_{AB} N)_{exp} \cdot (1 + 3.9 N^{2/3 - 2\nu})/N$ with $N = 64$ and $\nu = 0.588$ [51]. The incompatibility parameter χ_{AS} for the outer block and effective solvent particles was always set to $\chi_{AS} = 0$, which corresponds to $A_{AS} = 25$. Moreover, χ_{BS} was systematically varied between 0 and 7 with step ≈ 0.72, corresponding to A_{BS} in the range between 25

Table 2 Composition of investigated star diblock copolymers (PS-b-PB)$_3$

Sample	v_{PS} [L/mol]	v_{PB} [L/mol]	v_{total} [L/mol]	α_{PS}	α_{PB}	N
1	1.73	12.53	14.26	0.12	0.88	144
2	4.09	9.76	13.85	0.30	0.70	140
3	1.93	7.60	9.53	0.20	0.80	96

v_{PS} and v_{PB} are molar volumes of PS and PB, respectively, whereas v_{total} is the total molar volume of the TSP. N is the TSP's polymerization degree computed on the basis of PS reference segment volume, and α_{PS} and α_{PB} denote the resulting number fractions of the two components

and 50. Finally, note that the main goal of our simulations using such a coarse-grained model is not to quantitatively reproduce the change of star properties with increasing χ_{BS}, for which atomistic simulations with realistic solvent interactions would be necessary, but to qualitatively assess the effect of self-associations on the change of TSPs static and dynamic behavior.

Experimental results

We first focus on the effect of the outer PS-block fraction on the dynamic relaxation of the TSP system at low densities. In Fig. 1, we show the experimental ISFs at a fixed wave vector and various temperatures for the two samples with comparable total molar masses but with distinct PS weight fractions. The ISFs show two distinct trends upon changing temperature. At high temperatures, the ISFs show a single exponential decay that demonstrates the existence of individual stars in solution. However, when temperature is reduced below the cloud temperature of the outer-block, the ISF features a two-step decay which indicates the coexistence of two distinct populations in the system. The first decay (fast process) in the ISF is similar to the one observed at high temperatures and hence represents the

individual stars in solution. On the other hand, the second decay (slow process) taking place at longer times suggests the presence of larger aggregates (clusters of TSPs). The slow process becomes more pronounced as the temperature is decreased. Interestingly, the two-step decay in the ISF appears at a slightly higher temperature for the TSP with a larger PS-fraction.

To extract hydrodynamic sizes associated with the two processes in the solution, that is individual TSPs and clusters, the relaxation spectrum is calculated from the inverse Laplace transformation of the ISF using the constraint regularized method [43] discussed in Section 4. Typical results of such analysis for the TSPs with two different PS fractions at $T = 60$ °C and 30 °C are shown in Fig. 2. The relaxation spectrum at 60 °C shows a single peak, which is rather sharp, reflecting single exponential decay of the ISF mode. The position of the peak shifts to a slightly longer time for the TSP with a smaller PS fraction, indicating a larger hydrodynamic radius. At the lower temperature of 30 °C, the relaxation spectrum exhibits two well-separated peaks, as seen in Fig. 2b. Similarly to high temperatures, the position of the first peak shifts to a slightly longer time for the TSP with a smaller PS fraction, whereas the position of the second peak in both TSP samples is located at a
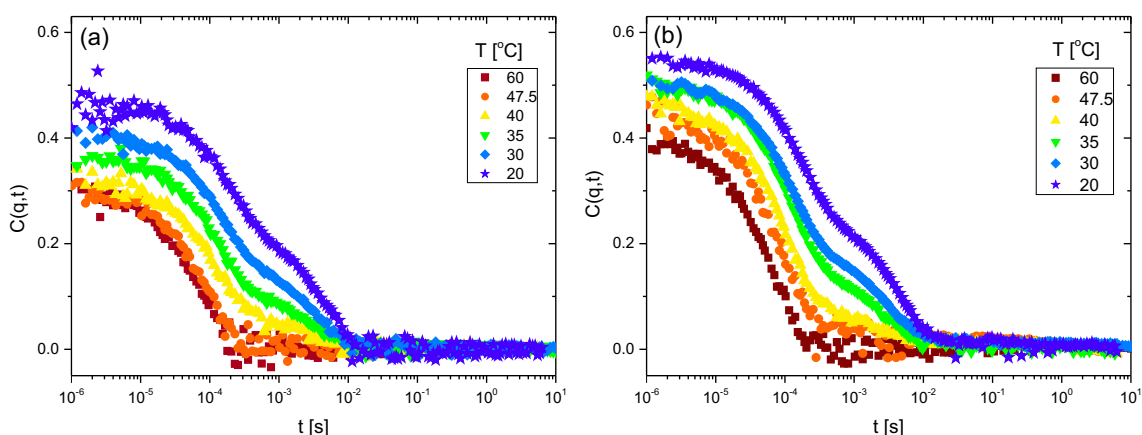

Fig. 1 Experimental ISFs at constant wave vector $q = 0.02475$ nm^{-1} and different temperatures for TSPs with the outer PS-block fractions of $f_{PS} = 0.14$ (**a**) and $f_{PS} = 0.33$ (**b**). Note that the plateau values of the ISF at short times are well below one. This is due to the fact that a part of the scattered intensity originates from density fluctuations of solvent molecules
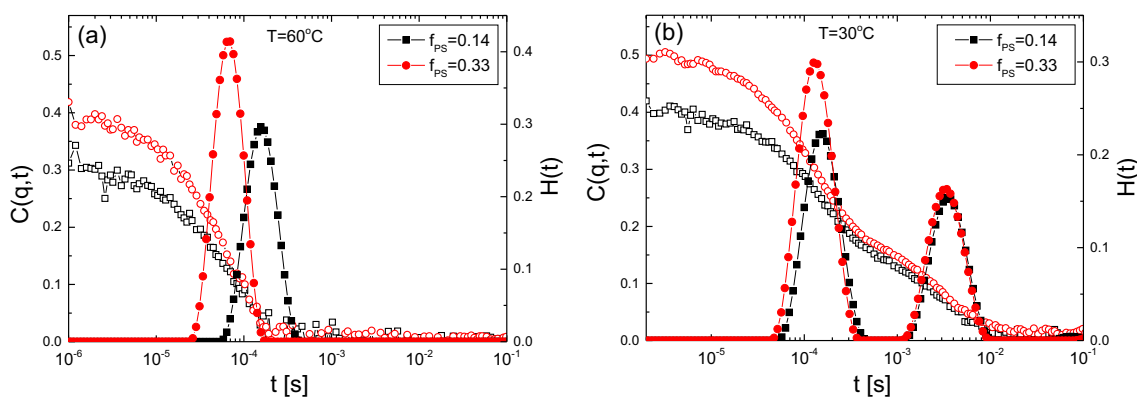
Fig. 2 ISF (open symbols, left axis) and its corresponding relaxation times spectrum (closed symbols, right axis) deduced from the constrained regularization method for the TSPs with PS fractions of $f_{PS} =$ 0.14 (black squares) and 0.33 (red circles) at $q = 0.02475$ nm^{-1} for $T = 60\,°C$ (**a**) and $T = 30\,°C$ (**b**)

similar time. These two peaks represent the relaxation times associated with individual TSPs and clusters, respectively. Subsequently, the two relaxation times are used to calculate the diffusion coefficients associated with each component. The diffusion coefficient for the fast mode (where $qR < 1$) is q-independent, whereas D for the slow mode (where $qR \geq 1$) shows some q-dependence. In the latter case, D extrapolated to $q = 0$ is used to calculate R_h. Then, the hydrodynamic sizes of TSPs and clusters are obtained using the Stokes-Einstein-Sutherland relation.

We first examine the effect of the block size ratio α on the single TSP size upon cooling. In experiments, the radius of gyration was too small to be probed by DLS. Instead, we focused on the hydrodynamic radius R_h of individual TSPs in dilute solution, as calculated from the fast process in the ISF using the Stokes-Einstein-Sutherland relation. The temperature dependence of R_h for the three studied TSP samples is shown in Fig. 3. The single star size exhibits a two-step shrinkage upon reducing temperature or

equivalently worsening the solvent quality. The first decay in size takes place at temperatures well below the cloud-point of outer PS-blocks, whereas the second drop is seen when temperature is reduced further below the cloud-point of the inner PB-block. Hence, the first decrease in size is associated with the collapse of outer blocks, whereas the second decay corresponds to the case when inner blocks start to collapse. At high temperatures, for the TSP with $f_{PS} = 0.14$, we find $R_h \approx 5$ nm and for $f_{PS} = 0.33$, $R_h \approx 4.6$ nm (see Fig. 3a). Although both TSPs have almost the same molar mass of about 40000 g/mol, the difference in their size originates from the difference in the fraction of PS. The radius of gyration of a star homopolymer in good solvent conditions is given by $R_g \approx \kappa(f)bN^\nu$, where $\nu = 0.588$, N is the number of Kuhn segments in a star arm, b is the size of a Kuhn segment, and $\kappa(f)$, which depends on the number of star arms f, is a numeric constant that takes into account the star functionality [52–54]. Using the latter relation, it can be found that the size of a star made of purely
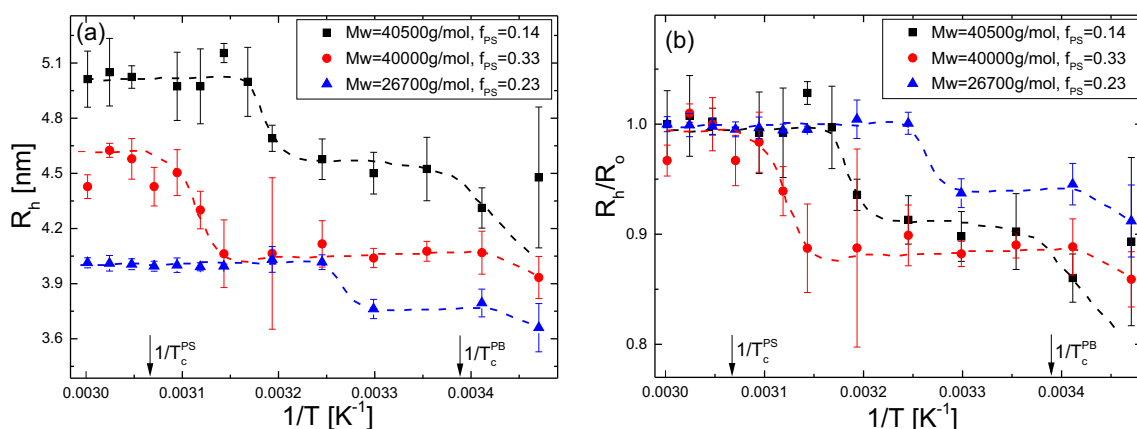

Fig. 3 **a** The hydrodynamic radius, R_h, of individual TSPs in the dilute solution calculated from the fast process in the experimentally determined ISFs. **b** R_h normalized by its plateau value at high temperatures.

The dashed lines serve as a guide to the eye. The black arrows indicate the cloud-points of inner PB and outer PS blocks

PB is about 65% larger compared with that made of purely PS, $R_g^{PB} \approx 1.65 R_g^{PS}$, given that their molar mass is the same [55]. Hence, it is expected that the increase in PS fraction reduces the size of a TSP. In order to compare the collapse process for stars of different size, we have normalized the TSP size by the plateau value of R_h at high temperatures.

The TSP with a larger fraction of outer PS-blocks ($f_{PS} = 0.33$) shows the first-step reduction in size at higher temperatures and the second-step drop at slightly lower temperatures compared with the TSP with a smaller PS fraction ($f_{PS} = 0.14$). In both stars, the decrease in size is about 15%, as seen in Fig. 3b. In addition, in Fig. 3, we show the results for a TSP with a smaller molar mass (26700 g/mol) with the outer PS-block fraction $f_{PS} = 0.23$, which is between the other two higher molar mass TSPs with $f_{PS} = 0.14$ and 0.33. The main difference is that the TSP with the smaller molar mass exhibits the decay in size at a much lower temperature compared with the other two, which originates from a smaller value of the incompatibility parameter $\sim \chi_{PS-S} N$. Moreover, the decrease in size is also rather weaker (about 10%), which can be attributed to a shorter length of its arms.

In Fig. 4, we present the temperature dependence of clusters' R_h for the systems of TSPs with the same molar mass but two different PS fractions ($M_W = 40000$ g/mol, $f_{PS} = 0.14$ and 0.33). In both TSPs, the cluster size shrinks on cooling. However, a slight but consistent increase in the cluster size is observed when temperature is further reduced below the cloud-point of the inner PB-block. Moreover, the hydrodynamic cluster size does not show change with the fraction of outer PS block. In Fig. 4a, we additionally show the results for the TSP with smaller molar mass ($M_W = 26700$ g/mol) and $f_{PS} = 0.23$. In this case, the temperature dependence of the cluster size is the same as for the other

two TSPs ($f_{PS} = 0.14, 0.33$). However, the smaller molar mass TSP shows a cluster size that is nearly three times larger. This could be due to a higher concentration of these TSPs. To rule out the effect of concentration, we have normalized the cluster size by the number density of TSPs in solution (Fig. 4b). The number density takes into account for the number of stickers available in the solution. With such normalization, the differences in cluster size between different TSPs are reduced to a great extent. The minor differences could originate from the complex nature of self-organization of TSPs due to differences in their molecular characteristics.

Simulation results

We now focus on static and dynamic properties of single TSPs under worsening solvent conditions for the outer B block, that is under increasing χ_{BS}. To do so, we simulated single stars with $f = 3$ arms of length $N = 64$ using a coarse-grained DPD model with explicit solvent particles, as described in detail in Section 4. The outer block ratio was systematically varied from 0.1 to 0.5 with step 0.1. The exact number of A- and B-type monomers in an arm was $N_A = 58, 52, 45, 39, 32$ and $N_B = 6, 12, 19, 25, 32$, respectively (the corresponding $\alpha = 0.1, 0.2, 0.3, 0.4, 0.5$). For each state point (α, χ_{BS}), we performed 10–12 independent simulation runs of length $10^5 \tau$, followed after a shorter equilibration period of $10^4 \tau$. Single TSPs were simulated in a box of size $L = 30 r_{cut}$ at the total particle density $\rho r_{cut}^3 = 3$. To check if such box size is sufficient to accommodate a TSP, we initially simulated the same star in good solvent conditions ($\chi_{BS} = 0$) in a larger box with $L = 35 r_{cut}$, and we did not observe any substantial changes
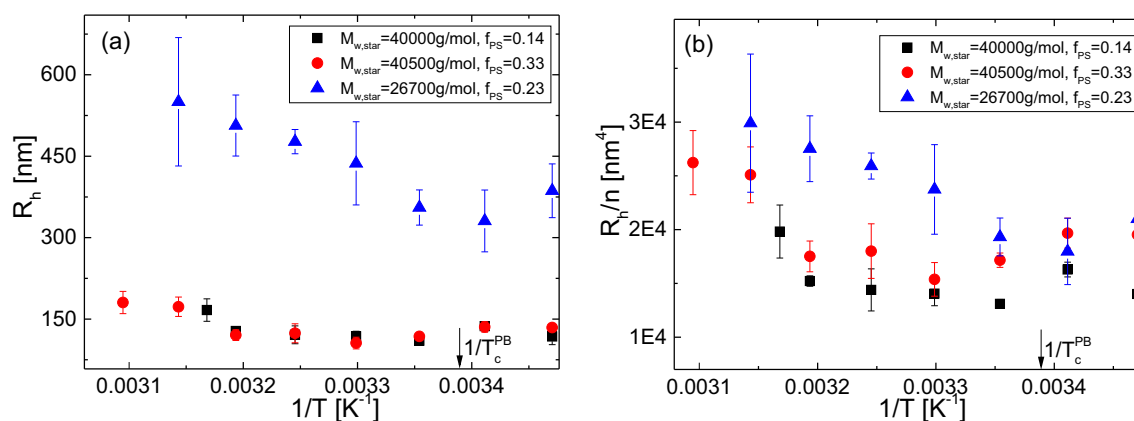

Fig. 4 **a** The hydrodynamic radius, R_h, of clusters extracted from the slow process in the experimental ISFs. **b** The ratio of R_h to the number density n (see Table 1) of TSPs in the solution. The black arrow indicates the cloud-point of inner PB blocks
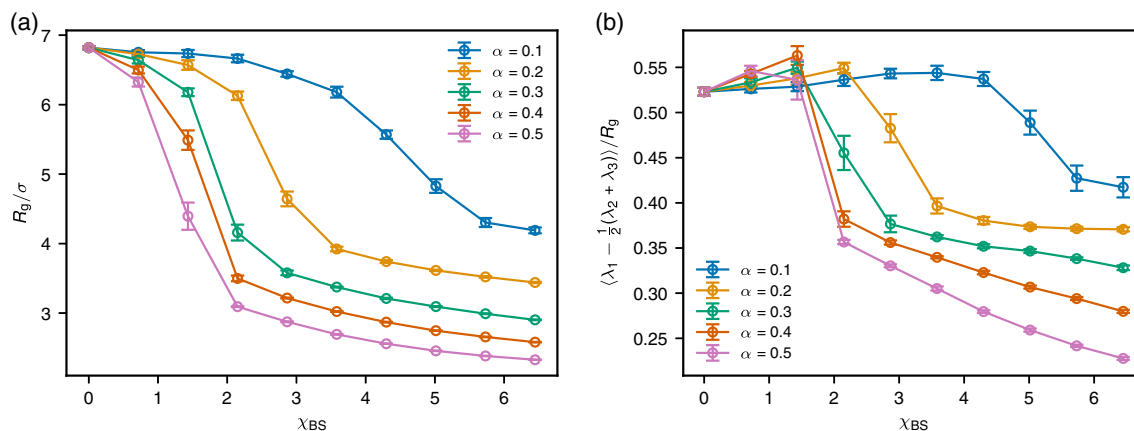
Fig. 5 **a** The mean radius of gyration of a TSP R_g as a function of χ_{BS} for different fractions of the outer block $\alpha = N_B/N$. **b** The mean asphericity of a TSP, computed as $\langle \lambda_1 - \frac{1}{2}(\lambda_2 + \lambda_3)\rangle$, scaled with its mean radius of gyration R_g as a function of χ_{BS} for different α

in its properties. In selective solvents, the TSP size is even smaller due to the formation of patches, which justifies the use of the same box size $L = 30 r_{cut}$ in this case.

To assess single star shape properties, we computed the eigenvalues λ_i ($i = 1, 2, 3, \lambda_1 \geq \lambda_2 \geq \lambda_3$) of the star's gyration tensor

$$G_{ij} = \frac{1}{fN+1} \sum_{k=1}^{fN+1} \Delta r_i^{(k)} \Delta r_j^{(k)}, \qquad (9)$$

where $\Delta r_i^{(k)}$ is the ith component of the kth monomer's position in the star's center of mass frame. In Fig. 5, we report the TSP's mean radius of gyration $R_g = \langle R_g^2 \rangle^{1/2}$ ($R_g^2 = \lambda_1 + \lambda_2 + \lambda_3$) as well as the mean asphericity parameter $\langle \lambda_1 - \frac{1}{2}(\lambda_2 + \lambda_3)\rangle$, which is positive and can vanish only for a completely symmetric configuration, as a function of χ_{BS} for different block length ratios α. The angles $\langle \cdots \rangle$ denote an ensemble and time average. We find that the behavior of a single TSP size is generally very similar to the experimental one (see Fig. 3): upon increasing χ_{BS}, we first observe a rather small decrease in R_g, followed by a major drop at higher χ_{BS}. Such behavior of R_g is associated with the formation of a single patch, where all three arms of a TSP clump together (see Fig. 6). We find that the transition point shifts towards a higher χ_{BS}, that is a lower temperature because $\chi \sim 1/T$, with decreasing α, which is in full accordance with the experimental behavior of the two samples with $f_{PS} = 0.14$ and 0.33 that have a very similar total molar mass (see Fig. 3b). Afterwards, only a small reduction of R_g is observed upon increasing χ_{BS}, as seen in Fig. 3a. We also note that simulations do not capture the second drop in size which is observed in experiments for temperatures below the cloud-point of inner-block. The reason for this discrepancy is that in simulation, for simplicity reasons, the inner-block is assumed to be always in a good solvency

condition. Hence, it only captures single step shrinkage process due to collapse of outer-block monomers.

We furthermore find that the final TSP size decreases with increasing α, also in accordance with the experimental findings for the samples with $f_{PS} = 0.14$ and 0.33 (see Fig. 3b). This behavior is associated with generally more open configuration of collapsed TSPs with small α that permit solvent flow through the TSP's interior. On the other hand, in the case of larger α, the solvophobic B-blocks form a single large patch that expels the solvent from its interior, resulting in more compact and symmetric configurations (see Figs. 6 and 5b). Interestingly, as can be seen in Fig. 5b, upon slightly increasing χ_{BS} from 0, the stars first become more aspherical, which can be attributed to the formation of transient patches between two out of three star arms. This is confirmed in Fig. 7 that reports the average number of patches formed by the star, the average number of arms in a patch, and the fraction of free arms as a function of χ_{BS} for different arm compositions. In agreement with earlier results [30], we find that such TSP with $f = 3$ forms only one patch for all α with all three arms contributing to it at high enough χ_{BS}. In addition, as seen from Fig. 7a and 7b, the point when all arms start to form a single patch
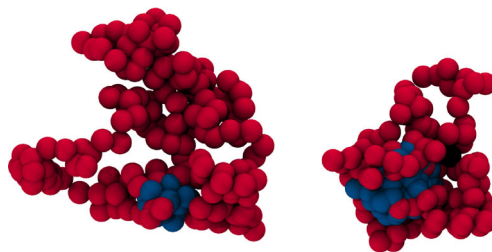

Fig. 6 Characteristic TSP conformations with $\alpha = 0.1$ (left) and $\alpha = 0.3$ (right) at a high $\chi_{BS} \approx 7$. B-monomers are blue, A-monomers—red, and star centers are black. Solvent particles are not shown for clarity
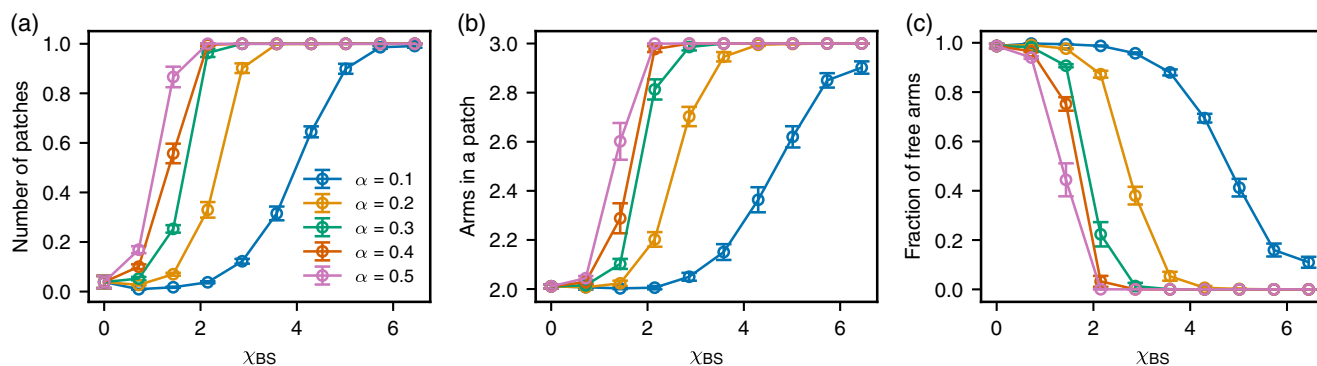
Fig. 7 a The total number of formed patches as a function of χ_{BS} for different α. Two arms are defined as being in a common patch if there is at least one pair of monomers from the two distinct arms lying at a distance $r \leq r_{cut}$. The average number of arms in a patch (**b**) and the average fraction of free arms (**c**) as a function of χ_{BS} for different α. **a**, **b**, and **c** share the same legend shown in (**a**)

corresponds to the point when R_g drops significantly (see Fig. 5a). Finally, to assess the influence of arm length N on the transition point for the watermelon-like structure formation, for $\alpha = 0.3$, we additionally simulated stars with arm length $N = 32, 48, 80$ for different values of χ_{BS}. The comparison between the behavior of the radius of gyration of TSPs with different N for $\alpha = 0.3$ is shown in Fig. 8. We find that the TSP with shorter arms features the star collapse at higher values of χ_{BS}, which therefore corresponds to lower temperatures in the experiments, being in line with the trend observed for the experimental sample with $f_{PS} = 0.23$ that has a lower molar mass, see Fig. 3.

The presence of faithful hydrodynamic interactions in DPD allows us to assess the influence of patch formation on the dynamics of single stars in solution. We did this by considering the mean-square displacement of TSP's center of mass, computed as:

$$\mathrm{MSD}(t) = \frac{1}{T-t} \int_0^{T-t} \left\langle [\mathbf{R}(t'+t) - \mathbf{R}(t')]^2 \right\rangle \, dt', \quad (10)$$

where $\mathbf{R}(t)$ is the position of the star's center of mass at time t, T is the total simulation time, and $\langle \cdots \rangle$ stands for the average over independent simulations runs. Typical behavior of the MSD for different α as well as the extracted diffusion coefficients D is shown in Fig. 9. We find that the tendency to form patches, causing more compact watermelon-like structures, increases the diffusivity of the TSP. In the experiments, this behavior corresponds to a reduction in the hydrodynamic radius R_h, which is in good agreement with results shown in Fig. 3. Furthermore, this effect is especially significant for the case of high α, where D at high χ_{BS} can become about two times bigger compared with athermal conditions with $\chi_{BS} = 0$, as seen in Fig. 9a, again in agreement with the experiments, where a larger reduction in R_h is seen for the TSP with a higher PS fraction. Finally, more open conformations of collapsed TSPs with low α make the increase in diffusivity less pronounced (for example, about 30% increase for $\alpha = 0.10$).

In addition, we have considered the dynamics of internal patch reorganizations at the single-star level. In Fig. 10, we show the times t_{free} for an arm spent in the free state, that is not forming an association with other arms, as a function of χ_{BS} for different α. We find that for all α, the mean value of t_{free} initially decreases exponentially fast with increasing χ_{BS} (Fig. 10a), up to a point where a single patch forms. At this point, $\langle t_{free} \rangle$ drops to 0, indicating that the single patch is stable over the course of the whole simulation. The value of χ_{BS} where it happens compares with the point where a significant reduction of R_g occurs (Fig. 5a). Furthermore, in Fig. 10b, we show the distribution for t_{free} for $\alpha = 0.1$ at various χ_{BS}, featuring tails that decay exponentially fast with increasing t_{free} in all cases.

Finally, we consider the formation of inter-star aggregates in the dilute solution. To asses such behavior, it is necessary to simulate a sufficiently large number of stars, which becomes computationally restrictive if using the model with
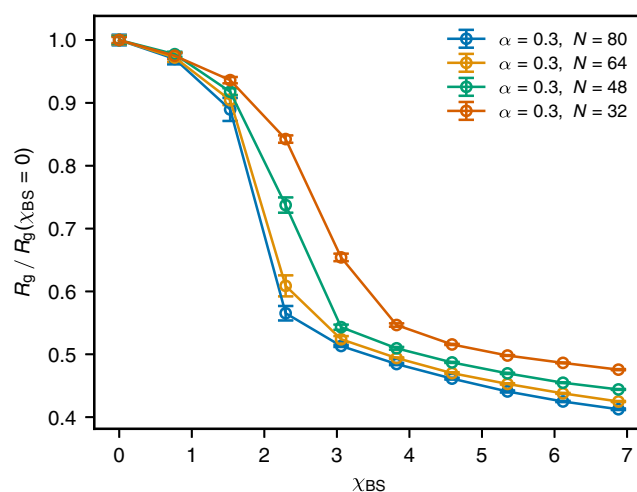

Fig. 8 The mean radius of gyration R_g of a TSP as a function of χ_{BS} for the same fraction of the outer block $\alpha = 0.3$ but different arm lengths N
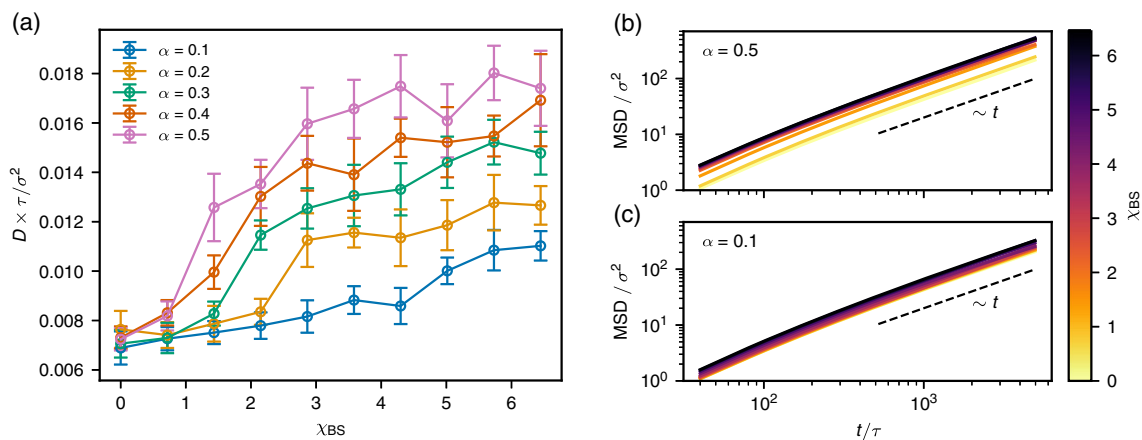
Fig. 9 **a** The diffusion coefficient D of the TSP's center of mass as a function of χ_{BS} for different α. D was extracted from the long-time behavior of the MSD of the star's center of mass, $MSD = 6Dt$. Typical MSD as a function of χ_{BS} are shown for $\alpha = 0.5$ (**b**) and $\alpha = 0.1$ (**c**)

$N = 64$ that was employed for single star behavior discussed previously. We therefore resort to an even coarser model with, similarly, $f = 3$ but with $N = 10$, and in what follows we focus on the case with $\alpha = 0.3$. We simulated 2000 such stars in a box with $L = 70r_{cut}$ at particle density $\rho r_{cut}^3 = 3$. In this model, the corresponding star concentration is $c \approx 0.4c^*$, which is higher than the one used in the experiments (to reach an equivalent experimental concentration of $c \approx 0.04c^*$, it would be necessary to simulate about a ten times bigger system containing $\sim 10^7$ particles). Nevertheless, even in this regime, we remain at concentrations considerably below c^*. Initially, TSPs were initialized uniformly in the box and subsequently equilibrated in athermal solvent conditions for both blocks with $\chi_{AS} = \chi_{BS} = 0$ (χ_{AB} was set to $\chi_{AB} = 28.6$ to match the experimental value $(\chi_{AB}N)_{eff} = 10$, as explained in Section 4). Afterward, the incompatibility parameter for the outer block was increased to 4.3 ($A_{BS} = 40$) over $2 \cdot 10^6$ integration time steps and then

further equilibrated for another $2 \cdot 10^6$ steps. During the latter stages, the TSPs initially began to form small micelles that subsequently merged into worm-like structures, which then again merged into a single giant cylindrical aggregate, shown in the left column of Fig. 11. Note that such cylindrical architecture is rather a consequence of periodic boundary conditions. It is likely that symmetric spherical aggregates would form in a more dilute system with a larger simulation box size, as, for instance, recently shown in Ref. [56]. Nonetheless, this illustrates the tendency of TSPs to form large aggregates even at dilute conditions, as previously shown in the experimental cluster sizes in Fig. 4. We also considered the effect of lowering temperature on the structure of such aggregate by quenching χ_{BS} to 10 ($A_{BS} = 60$) and equilibrating the system for another 10^6 integration time steps. As shown in the right column of Fig. 11, as a result of the χ_{BS} increase, the aggregate shrinks in the two transverse directions. This occurs because the solvophobic
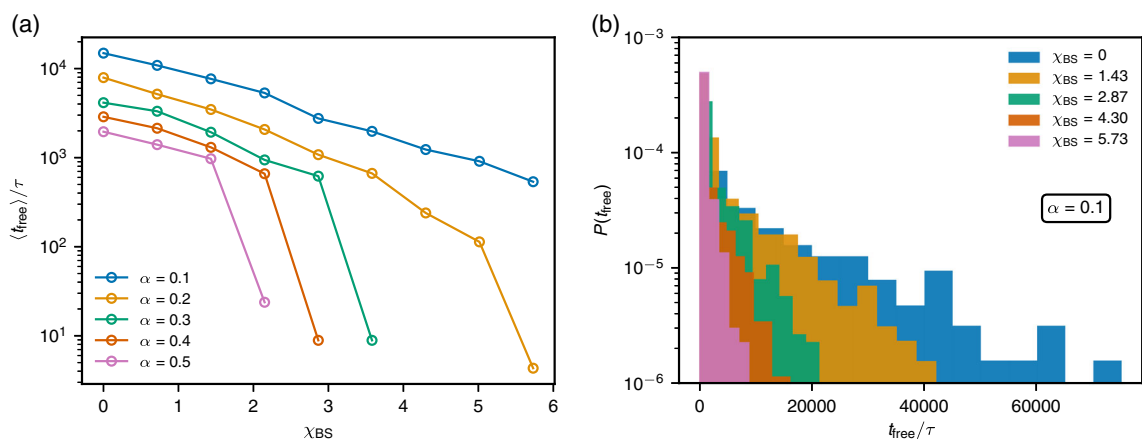

Fig. 10 **a** The mean time of an arm not belonging to a patch $\langle t_{free} \rangle$ as a function of χ_{BS} for different α. **b** The normalized distribution of t_{free} for $\alpha = 0.1$ and various χ_{BS}
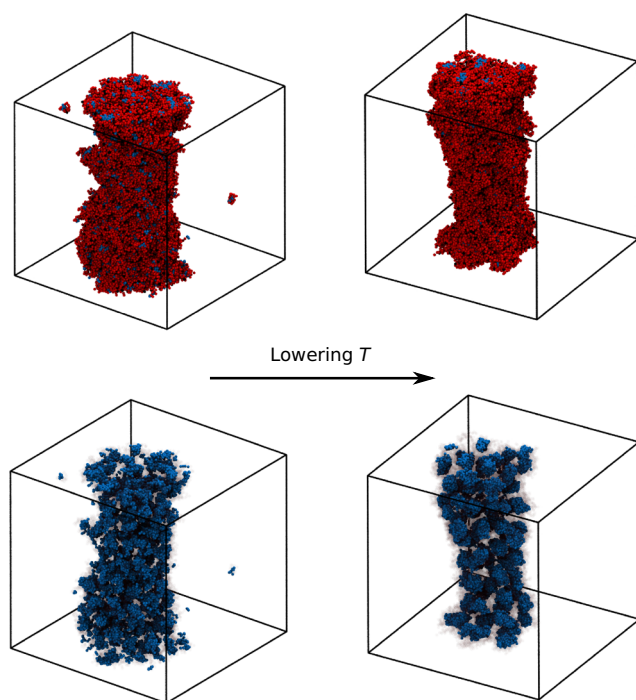
Fig. 11 Left column: self-assembly of three-arm TSPs with $N = 10$ and $\alpha = 0.3$ into a giant cylindrical aggregate at $c \approx 0.4c^*$. The bottom row shows only the solvophobic B-blocks. Right column: the aggregate shrinks in the transverse directions upon increasing the solvophobicity of the B-monomers that become more ordered (bottom image)

TSP blocks that lie in the aggregate's interior become more ordered and thus push away the remaining solvent (see the bottom row of Fig. 11). This further agrees with the experimental trend of decreasing cluster size with decreasing temperature (Fig. 4).

Conclusions

In summary, we have investigated the self-assembly of TSPs with a variable size of the outer block as well as the arm length, which are subject to worsening solvent conditions, in dilute solutions. We find that two distinct modes in the experimental ISF appear upon lowering the temperature below a critical value: the fast-relaxing mode that corresponds to free stars in solutions as well as a slow-relaxing mode that indicates the presence of large aggregates. We find that the size of both populations decreases upon cooling. For single TSPs, the decay is associated with the formation of a single patch, where all three arms come together. From both experiments and simulations, we find that the temperature that corresponds to such transition increases with growing fraction of solvophobic monomers. However, we find that the transition temperature increases with the polymerization degree of

TSP arms, when keeping the fraction of solvophobic monomers constant. The formed aggregates in solution are much bigger than single stars (~ 100 nm versus ~ 5 nm). In simulations, albeit at a higher concentration of TSPs, we have found the formation of micellar aggregates with complex internal structure. Upon worsening the solvent quality for the outer block, the solvent is becoming more strongly expelled from the aggregate's interior, which causes the reduction of its size, similarly to the experimental behavior. We therefore speculate that similar objects also form at concentrations similar to the experimental ones, in line with assembled structures that have been recently observed in large-scale DPD simulations of linear diblock co-polymers in dilute conditions [56].

Compliance with ethical standards

References

1. Pavlovic M, Antonietti M, Schmidt BV, Zeininger L (2020) J Colloid Interface Sci 575:88
2. Salonen A, Langevin D, Perrin P (2010) Soft Matter 6(21):5308
3. Vandenhaute M, Schelfhout J, Van Vlierberghe S, Mendes E, Dubruel P (2014) Eur Polym J 53:126
4. Dong J, Wang Y, Zhang J, Zhan X, Zhu S, Yang H, Wang G (2013) Soft Matter 9(2):370
5. Deng X, Livingston JL, Spear NJ, Jennings GK (2020) Langmuir 36(3):715
6. Fan TF, Park S, Shi Q, Zhang X, Liu Q, Song Y, Chin H, Ibrahim MSB, Mokrzecka N, Yang Y et al (2020) Nat Commun 11(1):1
7. Han P, Li S, Wang C, Xu H, Wang Z, Zhang X, Thomas J, Smet M (2011) Langmuir 27(23):14108
8. Balkenende DW, Monnier CA, Fiore GL, Weder C (2016) Nat Commun 7(1):1

9. Weiss LB, Nikoubashman A, Likos CN (2017) ACS Macro Lett 6(12):1426
10. Chubak I, Locatelli E, Likos CN (2018) Mol Phys 116(21-22):2911
11. Ahmadian Dehaghani Z, Chubak I, Likos CN, Ejtehadi MR (2020) Soft Matter 16:3029
12. Liebetreu M, Likos CN (2020) Comms Mater 1(1):4
13. Rauscher PM, Rowan SJ, de Pablo JJ (2018) ACS Macro Lett 7(8):938
14. Wu Q, Rauscher PM, Lang X, Wojtecki RJ, de Pablo JJ, Hore MJA, Rowan SJ (2017) Science 358(6369):1434
15. Moore NT, Lua RC, Grosberg AY (2004) Proc Natl Acad Sci U.S.A 101(37):13431
16. Slimani MZ, Bacova P, Bernabei M, Narros A, Likos CN, Moreno AJ (2014) ACS Macro Lett 3(7):611
17. Weiss LB, Likos CN, Nikoubashman A (2019) Macromolecules 52(20):7858
18. Rauscher PM, Schweizer KS, Rowan SJ, de Pablo JJ (2020) Macromolecules 53(9):3390
19. Smrek J, Chubak I, Likos CN, Kremer K (2020) Nat Commun 11(1):26
20. Klotz AR, Soh BW, Doyle PS (2020) Proc Natl Acad Sci U.S.A 117(1):121
21. Rosa A, Smrek J, Turner MS, Michieletto D (2020) ACS Macro Lett 9(5):743
22. Biffi S, Cerbino R, Nava G, Bomboi F, Sciortino F, Bellini T (2015) Soft Matter 11(16):3132
23. Mirkin CA, Letsinger RL, Mucic RC, Storhoff JJ (1996) Nature 382(6592):607
24. Dreyfus R, Leunissen ME, Sha R, Tkachenko AV, Seeman NC, Pine DJ, Chaikin PM (2009) Phys Rev Lett 102(4):048301
25. Angioletti-Uberti S, Mognetti BM, Frenkel D (2012) Nat Mater 11(6):518
26. Pitsikalis M, Hadjichristidis N, Mays JW (1996) Macromolecules 29(1):179
27. Broze G, Jérôme R, Teyssié P (1982) Macromolecules 15(3):920
28. Van Ruymbeke E, Vlassopoulos D, Mierzwa M, Pakula T, Charalabidis D, Pitsikalis M, Hadjichristidis N (2010) Macromolecules 43(9):4401
29. Vlassopoulos D, Pakula T, Fytas G, Pitsikalis M, Hadjichristidis N (1999) J Chem Phys 111(4):1760
30. Lo Verso F, Likos CN, Mayer C, Löwen H (2006) Phys Rev Lett 96:187802
31. Rovigatti L, Capone B, Likos CN (2016) Nanoscale 8:3288
32. Moghimi E, Chubak I, Statt A, Howard MP, Founta D, Polymeropoulos G, Ntetsikas K, Hadjichristidis N, Panagiotopoulos AZ, Likos CN, Vlassopoulos D (2019) ACS Macro Lett 8(7):766
33. Capone B, Coluzza I, LoVerso F, Likos CN, Blaak R (2012) Phys Rev Lett 109:238301
34. Koch C, Likos CN, Panagiotopoulos AZ, Lo Verso F (2011) Mol Phys 109(23-24):3049
35. Lo Verso F, Panagiotopoulos AZ, Likos CN (2009) Phys Rev E 79:010401
36. Lo Verso F, Panagiotopoulos AZ, Likos CN (2010) Faraday Discuss 144:143
37. Koch C, Panagiotopoulos AZ, Lo Verso F, Likos CN (2013) Soft Matter 9:7424
38. Koch C, Panagiotopoulos AZ, Lo Verso F, Likos CN (2015) Soft Matter 11:3530
39. Geerissen H, Wolf BA (1982) Chem Rapid Commun 3(1):17
40. Berne BJ, Pecora R (2000) *Dynamic* Light Scattering: with Applications to Chemistry, Biology and Physics (Courier Corporation)
41. Kroeger A, Belack J, Larsen A, Fytas G, Wegner G (2006) Macromolecules 39(20):7098
42. Bockstaller M, Köhler W, Wegner G, Vlassopoulos D, Fytas G (2001) Macromolecules 34(18):6359
43. Provencher SW (1982) Comput Phys Commun 27(3):229
44. Groot RD, Warren PB (1997) J Chem Phys 107(11):4423
45. Anderson JA, Lorenz CD, Travesset A (2008) J Comput Phys 227(10):5342
46. Glaser J, Nguyen TD, Anderson JA, Lui P, Spiga F, Millan JA, Morse DC, Glotzer SC (2015) Comput Phys Commun 192:97
47. Howard MP, Panagiotopoulos AZ, Nikoubashman A (2018) Comput Phys Commun 230:10
48. Phillips CL, Anderson JA, Glotzer SC (2011) J Comput Phys 230(19):7191
49. Verlet L (1967) Phys Rev 159:98
50. Wolff T, Burger C, Ruland W (1993) Macromolecules 26(7):1707
51. Groot RD, Madden TJ (1998) J Chem Phys 108(20):8713
52. Likos CN (2001) Phys Rep 348(4):267
53. Daoud M, Cotton J (1982) J Phys France 43(3):531
54. Hsu HP, Nadler W, Grassberger P (2004) Macromolecules 37(12):4658
55. Rubinstein M, Colby RH (2003) Polymer physics. Oxford University Press, New York
56. Ye X, Khomami B (2020) Soft Matter 16:6056